12-2012

An Investigation Into Using Magnetically Attached Piezoelectric Elements for Vibration Control

J. C. Collinger
Bechtel Marine Propulsion Corporation

W. C. Messner
Carnegie Mellon University

Jonathan A. Wickert
Iowa State University, wickert@iastate.edu

An Investigation Into Using Magnetically Attached Piezoelectric Elements for Vibration Control

Abstract

A novel vibration control method utilizing magnetically mounted piezoelectric elements is described. Piezoelectric elements are bonded to permanent magnets, termed here as control mounts, which are attached to the surface of a steel beam through their magnetic attraction. The magnetic-piezoelectric control mounts are an alternative to traditional epoxy attachment methods for piezoelectric elements which allows for easy in-the-field reconfiguration. In model and laboratory measurements, the beam is driven through base excitation and the resonant shunt technique is utilized to demonstrate the attenuation characteristics of two magnetic-piezoelectric control mounts. The coupled system is discretized using a Galerkin finite element model that incorporates the tangential and vertical contact stiffnesses of the beam-magnet interface. The vibration reduction provided by the control mounts using a single magnet are compared to those designed with a magnetic array that alternates the magnetic dipoles along the length of the mount. Even though each design uses the same magnet thickness, the alternating magnetic configuration's interfacial contact stiffness is over 1.5 and 4 times larger in the tangential and vertical directions, respectively, than that of the single magnet, resulting in increased vibration reduction. Measured and simulated results show that the magnetic-piezoelectric control mounts reduced the beam's tip velocity by as much as 3.0 dB and 3.1 dB, respectively. The design tradeoffs that occur when replacing the traditional epoxy layer with a magnet are also presented along with some methods that could improve the vibration reduction performance of the control mounts. This analysis shows that the control mounts attenuate significant vibration despite having an imperfect bond with the beam, thus providing a viable and adaptable alternative to traditional piezoelectric attachment methods.

Disciplines

Acoustics, Dynamics, and Controls | Mechanical Engineering

Comments

This article is from *Journal of Vibration and Acoustics* 134, no. 6 (December 2012): 061008, doi:10.1115/1.4007021.

An Investigation Into Using Magnetically Attached Piezoelectric Elements for Vibration Control

J. C. Collinger[1]
Bechtel Marine Propulsion Corporation,
West Mifflin, PA, 15122
e-mail: john.c.collinger@gmail.com

W. C. Messner
Department of Mechanical Engineering,
Carnegie Mellon University,
Pittsburgh, PA, 15213

J. A. Wickert
Dean
College of Engineering,
Iowa State University,
Ames, IA, 50011

A novel vibration control method utilizing magnetically mounted piezoelectric elements is described. Piezoelectric elements are bonded to permanent magnets, termed here as control mounts, which are attached to the surface of a steel beam through their magnetic attraction. The magnetic-piezoelectric control mounts are an alternative to traditional epoxy attachment methods for piezoelectric elements which allows for easy in-the-field reconfiguration. In model and laboratory measurements, the beam is driven through base excitation and the resonant shunt technique is utilized to demonstrate the attenuation characteristics of two magnetic-piezoelectric control mounts. The coupled system is discretized using a Galerkin finite element model that incorporates the tangential and vertical contact stiffnesses of the beam-magnet interface. The vibration reduction provided by the control mounts using a single magnet are compared to those designed with a magnetic array that alternates the magnetic dipoles along the length of the mount. Even though each design uses the same magnet thickness, the alternating magnetic configuration's interfacial contact stiffness is over 1.5 and 4 times larger in the tangential and vertical directions, respectively, than that of the single magnet, resulting in increased vibration reduction. Measured and simulated results show that the magnetic-piezoelectric control mounts reduced the beam's tip velocity by as much as 3.0 dB and 3.1 dB, respectively. The design tradeoffs that occur when replacing the traditional epoxy layer with a magnet are also presented along with some methods that could improve the vibration reduction performance of the control mounts. This analysis shows that the control mounts attenuate significant vibration despite having an imperfect bond with the beam, thus providing a viable and adaptable alternative to traditional piezoelectric attachment methods. [DOI: 10.1115/1.4007021]

1 Introduction

Piezoelectric elements, most notably lead zirconate titanate (PZT), attenuate vibration by transferring energy between the mechanical and electrical domains of the material. A voltage develops across the electrodes when the material deforms and conversely, the elements strain when a voltage is applied across their electrodes. In passive vibration control applications, the piezoelectric elements are attached to a vibrating structure, and as they deform, energy is dissipated as current is driven through a shunt connected to its electrodes. The electrical components that comprise the shunt directly impact the current output, and thus energy dissipation, of the piezoelectric control techniques. While various passive control methods utilize resistive [1–4] and capacitive [5] shunts, the most effective is the resistive-inductive, or resonant, shunt [6–10] which couples with the piezoelectric capacitance to form an oscillatory circuit. When the resonant shunt is tuned to a mechanical resonance of the base structure, current and energy dissipation are maximized. Other types of control techniques include the state-switching [11] and synchronized switching techniques [12–17], which are semipassive approaches to piezoelectric vibration control, in which the piezoelectric stiffness is varied intermittently throughout the structure's period of vibration. In addition, active vibration control techniques use the elements to oppose the motion of the vibrating beam at its resonant frequencies [18].

The spatial configuration of the elements plays an important role in the efficacy of the piezoelectric vibration control techniques. An accurate modal analysis of the structure is required a priori to ensure that the elements are attached away from the nodal lines of a particular mode of interest and positioned in regions that maximize their modal controllability [19,20]. Placement in these regions maximizes the electromechanical coupling between the elements and the vibrating structure, thereby increasing the efficiency of the techniques. These areas are well known for simple structures like beams [21–23] and plates [24]. However, for more complex systems, it can be difficult to precisely model the structural dynamics of such systems and to completely capture the environmental effects that influence the system's response over time. In addition, since the elements typically are bonded to the surface of the structure using epoxy [1,3,6,7,9,10,13,14], it is costly and difficult to reconfigure the elements should a change be required, or if the elements become damaged.

In what follows, a piezoelectric attachment method in which permanent magnets are used to replace the traditional epoxy bond is demonstrated. Previous work has shown that these novel devices, termed here as control mounts, provide the flexibility of easy in-the-field reconfiguration while still exhibiting the attachment strength to dissipate energy using the piezoelectric elements [25–27]. The magnetic-piezoelectric control mounts, comprised of piezoelectric elements bonded to magnets, are attached to a steel beam through their magnetic attraction to control the response of the beam. The equations of motion for such a system are developed using a Hamiltonian analysis that incorporates the relative axial and lateral motion between the beam and the mounts. The axial and lateral displacements of the beam and the control mounts are determined through a Galerkin finite element model. The mounts'

[1]Corresponding author.

Contributed by the Technical Committee on Vibration and Sound of ASME for publication in the JOURNAL OF VIBRATION AND ACOUSTICS. Manuscript received February 15, 2011; final manuscript received March 28, 2012; published online October 29, 2012. Assoc. Editor: Ranjan Mukherjee.

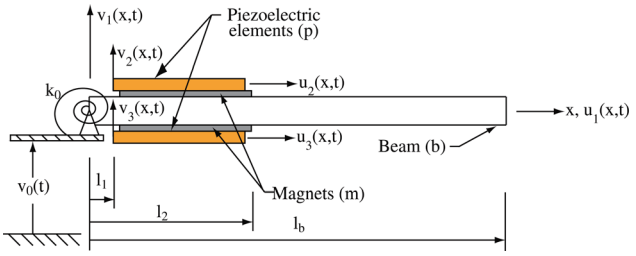

Fig. 1 Illustration of a pinned-free beam, subjected to excitation at the base with torsional stiffness k_0 and with magnetically mounted piezoelectric elements

damping characteristics are demonstrated using the resonant shunt control technique, and when subjected to such control, the mechanical and electrical systems couple and the displacements are readily solved. Simulated and experimental results are presented as well as a discussion on the vibration reduction performance of the control mounts. In addition, the design tradeoffs that occur when replacing the traditional epoxy layer with a magnet are presented along with some methods that could improve the vibration reduction performance of the control mounts.

2 Vibration Model

Figure 1 illustrates a pinned-free Euler-Bernoulli beam subject to excitation v_0 at the base with torsional stiffness k_0. The beam's lateral motion is given as $v_0(t) + v_1(x,t)$, where $v_1(x,t)$ measures the beam's displacement relative to the base. Two control mounts, which are comprised of magnets assumed to be perfectly bonded to piezoelectric elements, are attached to the steel beam through their magnetic attraction over the region (l_1, l_2) in a bimorph configuration. The beam b, each magnet m, and each piezoelectric element p, are rectangular with cross-sectional areas $A_i = w_i h_i$, where w_i and h_i denote widths and thicknesses, and $i = b$, m, or p. The second moments of area about their respective neutral axes are denoted as I_b, I_m, and I_p, the moduli as E_b, E_m, and E_p, and the volumetric densities as ρ_b, ρ_m, and ρ_p. Numerical values used for the model parameters in simulation are listed in Table 1. The control mounts have mass per unit length $\rho A_c(x) = \rho A_m(x) + \rho A_p(x)$, axial stiffness $EA_c(x) = EA_m(x) + EA_p(x)$, and bending stiffness $EI_c = EI_m(x) + EI_p(x)$, and their neutral axes are located at a distance

$$h_n = \frac{EA_m h_m/2 + EA_p(h_m + h_p/2)}{EA_m + EA_p} \tag{1}$$

away from beam-magnetic interfaces, as illustrated in Fig. 2. The distance $h_{pd} = h_p/2 + h_m - h_n$ denotes the distance between the mid-thickness of the piezoelectric elements and the neutral axis of the control mount.

The beam-magnet attachment strength is dependent upon the interfacial normal and tangential forces developed between the beam and the control mounts. For low excitation amplitudes, the interfacial normal forces

$$N_{12} = k_v(v_2 - v_1) \quad \text{and} \quad N_{13} = k_v(v_1 - v_3) \tag{2}$$

vary linearly with the vertical contact stiffness per unit length k_v [28], where $v_2(x,t)$ and $v_3(x,t)$ are the top and bottom control mounts' lateral displacements, respectively. The interfacial tangential force depends upon the relative axial motion between the control mounts and the beam, and can assume different functional forms if the interface experiences pure sticking or a combination of sticking and slipping [29,30]. However, for the small excitation amplitudes and magnetic attraction forces used in this work, the interfaces are assumed to only experience sticking. In the light of this, the tangential forces per unit length

Table 1 Properties of parameters used in simulations

Description	Symbol	Value
Beam		
Volumetric density	ρ_b	7.87×10^3 kg/m^3
Young's modulus	E_b	200 GPa
Length	l_b	20.32 cm
Width	w_b	1.27 cm
Thickness	h_b	0.32 cm
Relative permeability	μ_r	696
Piezoelectric elements		
Volumetric density	ρ_b	7.80×10^3kg/m^3
Young's modulus	E_b	66GPa
Length	l_p	2.53 cm
Width	w_p	1.27 cm
Thickness	h_p	0.24 cm
Charge constant	d_p	-1.75×10^{-10} m/V
Dielectric constant	ε_3^s	1.48×10^{-8} F/m
Magnetic arrays		
Volumetric density	ρ_m	7.50×10^3 kg/m^3
Young's modulus	E_m	166 GPa
Length	l_m	2.53 cm
Width	w_m	1.27 cm
Thickness	h_m	0.16 cm
Coercive force	H_c	8.76×10^5 A/m
Relative permeability	μ_r	1

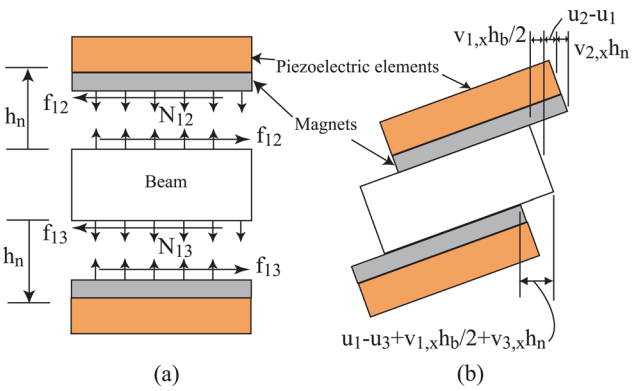

Fig. 2 Illustration of the (*a*) interfacial normal and tangential forces and (*b*) relative axial displacement at the control mount-beam interface

$$f_{12} = k_t\left(u_2 - u_1 + \frac{h_b}{2}v_{1,x} + h_n v_{2,x}\right) \tag{3}$$

and

$$f_{13} = k_t\left(u_1 - u_3 + \frac{h_b}{2}v_{1,x} + h_n v_{3,x}\right) \tag{4}$$

depend upon the relative axial displacements [31–33], where $u_1(x,t)$, $u_2(x,t)$, and $u_3(x,t)$ are the beam's and control mounts' axial displacements, and k_t is the tangential contact stiffness per unit length [30]. The notation $v_{1,x}$ denotes the partial derivative of v_1 with respect to x.

2.1 Galerkin Formulation. The equations of axial and lateral motion of the beam and control mounts are derived using Hamilton's principle for coupled electromechanical systems [34]

$$\int_{t_1}^{t_2}\left[\delta\left(T_b + T_c - U_b - U_c + W_e + W_N + W_f\right) - \delta V q_a\right]dt = 0 \tag{5}$$

with the kinetic energy of the beam

$$T_b = \frac{1}{2}\int_0^{l_b} \rho A_b \left(u_{1,t}^2 + \left(v_{,t} + \dot{v}_0\right)^2\right) dx \tag{6}$$

and of the magnetic-piezoelectric control mounts

$$T_c = \frac{1}{2}\int_0^{l_b} \rho A_c(x) \left(u_{2,t}^2 + u_{3,t}^2 + v_{2,t}^2 + v_{3,t}^2\right) H(x) dx \tag{7}$$

consisting of both the axial and lateral velocities of the system, where $H(x) = H_1(x - l_1) - H_2(x - l_2)$ is a combination of Heaviside step functions. A portion of the system's potential energy is separated into the beam's stored energy

$$U_b = \frac{1}{2}\int_0^{l_b} EI_b v_{1,xx}^2 dx + \frac{1}{2} k_0 v_{1,x}(0,t)^2 \tag{8}$$

which consists of its strain energy and the energy stored in the torsional spring. Additionally, there is potential energy

$$U_c = \frac{1}{2}\int_0^{l_b} \left[EA_c(x)\left(u_{2,x}^2 + u_{3,x}^2\right) + EI_c(x)\left(v_{2,xx}^2 + v_{3,xx}^2\right) + d_p E_p w_p V\left(u_{2,x} - u_{3,x} - h_{pd}\left(v_{2,xx} + v_{3,xx}\right)\right)\right] H(x) dx \tag{9}$$

stored in the control mounts, and work

$$W_e = \frac{1}{2}\int_0^{l_b} \left[d_p E_p w_p V\left(-u_{2,x} + u_{3,x} + h_{pd}\left(v_{2,xx} + v_{3,xx}\right)\right) + \frac{2\epsilon_3^s w_p}{h_p} V^2\right] H(x) dx \tag{10}$$

is also performed by the electric field of piezoelectric elements, which are calculated using the strain-charge piezoelectric constitutive equations [35] and assuming a constant electric field V/h_p in the opposite direction within the top and bottom piezoelectric elements, respectively. The virtual work $-\delta V q_a$ arises from an applied charge on the piezoelectric elements, where V is the voltage measured across the electrodes and the virtual works

$$\delta W_N = -\int_0^{l_b} \left[N_{12}(\delta v_2 - \delta v_1) + N_{13}(\delta v_1 - \delta v_3)\right] H(x) dx \tag{11}$$

and

$$\delta W_f = -\int_0^{l_b} \left[f_{12}\left(\delta u_2 - \delta u_1 + \frac{h_b}{2}\delta v_{1,x} + h_n \delta v_{2,x}\right) + f_{13}\left(\delta u_1 - \delta u_3 + \frac{h_b}{2}\delta v_{1,x} + h_n \delta v_{3,x}\right)\right] H(x) dx \tag{12}$$

account for the interfacial normal and tangential forces, respectively, between the control mounts and the beam. Energy dissipation is assumed to either be from viscous damping, or from heat dissipation as current is driven through an electrical shunt by the piezoelectric elements. Both of these mechanisms will be discussed in future sections.

The system's dynamic response is determined using a Galerkin finite element discretization with the axial and lateral displacements approximated over each element, respectively, as

$$u_j = \sum_{i=1}^{2} \psi_{ji}^e(\xi)\eta_{ji}^e(t) \quad \text{for} \quad \mathrm{j} = 1,2,3 \tag{13}$$

and

$$v_j = \sum_{i=1}^{4} \psi_{ji}^e(\xi)\eta_{ji}^e(t) \quad \text{for} \quad \mathrm{j} = 4,5,6 \tag{14}$$

where $\xi = (x - x_k)/l_e$ is the local coordinate over each element illustrated in Fig. 3, the $\eta_{ji}^e(t)$s are the nodal displacements and rotations, and there are n total elements of length $l_e = l_b/n$. The shape functions

$$\psi_{j1}^e(\xi) = 1 - \xi \quad \text{and} \quad \psi_{j2}^e(\xi) = \xi \quad \text{for} \quad \mathrm{j} = 1,2,3 \tag{15}$$

are used to determine the axial displacements, and the local cubic Hermite shape functions

$$\psi_{j1}^e(\xi) = 1 - 3\xi^2 + 2\xi^3, \quad \psi_{j2}^e(\xi) = l_e\left(\xi - 2\xi^2 + \xi^3\right)$$
$$\psi_{j3}^e(\xi) = 3\xi^2 - 2\xi^3, \quad \psi_{j4}^e(\xi) = l_e\left(-\xi^2 + \xi^3\right) \quad \text{for} \quad \mathrm{j} = 4,5,6 \tag{16}$$

approximate the lateral displacements [36]. The equations of motion are determined by applying Hamilton's principle with the elemental approximations of Eqs. (13) and (14) and allowing arbitrary variations in the nodal displacements and rotations. Upon discretization, the global response of the coupled system is approximated by

$$\mathbf{M}\ddot{\boldsymbol{\eta}} + \left(\mathbf{K^s} + \mathbf{K^{tv}} + C_p \Theta\Theta^T\right)\boldsymbol{\eta} = \mathbf{F} + \Theta q_a \tag{17}$$

where the global mass matrix

$$\mathbf{M} = \mathrm{diag}(\mathbf{M_{ii}}) \quad \text{for} \quad \mathrm{i} = 1,2,\ldots,6 \tag{18}$$

the global structural stiffness matrix

$$\mathbf{K^s} = \mathrm{diag}\left(\mathbf{K_{ii}^s}\right) \quad \text{for} \quad \mathrm{i} = 1,2,\ldots,6 \tag{19}$$

the global contact stiffness matrix

$$\mathbf{K^{tv}} = \begin{bmatrix} \mathbf{K_{11}^t} & \mathbf{K_{12}^t} & \mathbf{K_{13}^t} & \mathbf{0} & \mathbf{K_{15}^t} & \mathbf{K_{16}^t} \\ & \mathbf{K_{22}^t} & \mathbf{0} & \mathbf{K_{24}^t} & \mathbf{K_{25}^t} & \mathbf{0} \\ & & \mathbf{K_{33}^t} & \mathbf{K_{34}^t} & \mathbf{0} & \mathbf{K_{36}^t} \\ & \mathrm{sym} & & \left(\mathbf{K_{44}^t} + \mathbf{K_{44}^v}\right) & \left(\mathbf{K_{45}^t} + \mathbf{K_{45}^v}\right) & \left(\mathbf{K_{46}^t} + \mathbf{K_{46}^v}\right) \\ & & & & \left(\mathbf{K_{55}^t} + \mathbf{K_{55}^v}\right) & \mathbf{0} \\ & & & & & \left(\mathbf{K_{66}^t} + \mathbf{K_{66}^v}\right) \end{bmatrix} \tag{20}$$

and the global force and electromechanical coupling vectors, respectively,

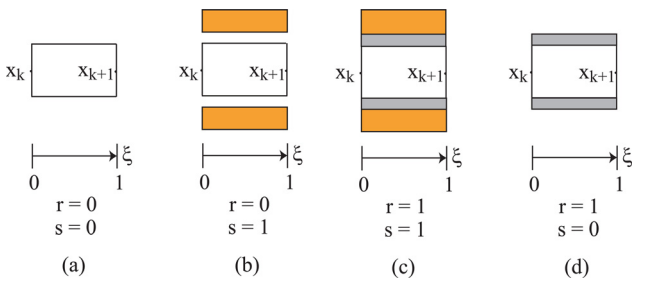

Fig. 3 The different local elements used in the finite element discretization along with the magnet *r* and piezoelectric *s* indices: (*a*) beam only, (*b*) beam with only the piezoelectrics, (*c*) beam with the magnets and piezoelectrics, and (*d*) beam with only the magnets

$$\mathbf{F} = \begin{bmatrix} \mathbf{0} \\ \mathbf{0} \\ \mathbf{0} \\ \mathbf{F_4} \\ \mathbf{0} \\ \mathbf{0} \end{bmatrix} \quad \text{and} \quad \mathbf{\Theta} = \begin{bmatrix} \mathbf{0} \\ \mathbf{\Theta_2} \\ \mathbf{\Theta_3} \\ 0 \\ \mathbf{\Theta_5} \\ \mathbf{\Theta_6} \end{bmatrix} \tag{21}$$

are built-up from the elemental matrices and vectors in the standard finite element procedure with proper boundary condition application, and where C_p denotes the piezoelectric capacitance.

2.2 Elemental System. Figure 3 shows the four different types of elements for the system along with the magnet and piezoelectric indices, r and s, respectively, which are unity whenever either material is present along the length of the beam and are zero otherwise. Using the shape functions in Eqs. (15) and (16), the axial and lateral elemental mass matrices, respectively, are

$$\begin{Bmatrix} \mathbf{M_{11}^e} \\ \mathbf{M_{22}^e} \\ \mathbf{M_{33}^e} \end{Bmatrix} = \begin{Bmatrix} \rho_b A_b \\ r\rho A_m + s\rho A_p \\ r\rho A_m + s\rho A_p \end{Bmatrix} \begin{bmatrix} 2 & 1 \\ 1 & 2 \end{bmatrix} \frac{l_e}{6} \tag{22}$$

and

$$\begin{Bmatrix} \mathbf{M_{44}^e} \\ \mathbf{M_{55}^e} \\ \mathbf{M_{66}^e} \end{Bmatrix} = \begin{Bmatrix} \rho_b A_b \\ r\rho A_m + s\rho A_p \\ r\rho A_m + s\rho A_p \end{Bmatrix} \begin{bmatrix} 156 & 22l_e & 54 & -13l_e \\ 22l_e & 4l_e^2 & 13l_e & -3l_e^2 \\ 54 & 13l_e & 156 & -22l_e \\ -13l_e & -3l_e^2 & -22l_e & 4l_e^2 \end{bmatrix} \frac{l_e}{420} \tag{23}$$

where each axial and lateral mass matrix is of the same form but with a different mass per unit length. Similarly, the axial and lateral elemental structural stiffness matrices are defined as

$$\begin{Bmatrix} \mathbf{K_{11}^{se}} \\ \mathbf{K_{22}^{se}} \\ \mathbf{K_{33}^{se}} \end{Bmatrix} = \begin{Bmatrix} E_b A_b \\ rEA_m + sEA_p \\ rEA_m + sEA_p \end{Bmatrix} \begin{bmatrix} 1 & -1 \\ -1 & 1 \end{bmatrix} \frac{1}{l_e} \tag{24}$$

and

$$\begin{Bmatrix} \mathbf{K_{44}^{se}} \\ \mathbf{K_{55}^{se}} \\ \mathbf{K_{66}^{se}} \end{Bmatrix} = \begin{Bmatrix} E_b I_b \\ rEI_m + sEI_p \\ rEI_m + sEI_p \end{Bmatrix} \begin{bmatrix} 12 & 6l_e & -12 & 6l_e \\ 6l_e & 4l_e^2 & -6l_e & 2l_e^2 \\ -12 & -6l_e & 12 & -6l_e \\ 6l_e & 2l_e^2 & -6l_e & 4l_e^2 \end{bmatrix} \frac{1}{l_e^3} \tag{25}$$

The contact stiffness matrix is partly composed of the elemental tangential stiffness matrices,

$$\begin{Bmatrix} \mathbf{K_{11}^{te}} \\ \mathbf{K_{22}^{te}} \\ \mathbf{K_{33}^{te}} \end{Bmatrix} = r \begin{Bmatrix} 2k_t \\ k_t \\ k_t \end{Bmatrix} \begin{bmatrix} 2 & 1 \\ 1 & 2 \end{bmatrix} \frac{l_e}{6} \tag{26}$$

and

$$\begin{Bmatrix} \mathbf{K_{44}^{te}} \\ \mathbf{K_{55}^{te}} \\ \mathbf{K_{66}^{te}} \end{Bmatrix} = r \begin{Bmatrix} 2k_t (h_b/2)^2 \\ k_t h_n^2 \\ k_t h_n^2 \end{Bmatrix} \begin{bmatrix} 36 & 3l_e & -36 & 3l_e \\ 3l_e & 4l_e^2 & -3l_e & -l_e^2 \\ -36 & -3l_e & 36 & -3l_e \\ 3l_e & -l_e^2 & -3l_e & 4l_e^2 \end{bmatrix} \frac{1}{30l_e} \tag{27}$$

which account for the axial and lateral tangential stiffness components, respectively. The off diagonal elemental stiffness matrices

$$\mathbf{K_{12}^{te}} = \mathbf{K_{13}^{te}} = -rk_t \begin{bmatrix} 2 & 1 \\ 1 & 2 \end{bmatrix} \frac{l_e}{6} \tag{28}$$

$$\mathbf{K_{15}^{te}} = -\mathbf{K_{16}^{te}} = -\mathbf{K_{25}^{te}} = \mathbf{K_{36}^{te}} = -rk_t h_n \begin{bmatrix} -6 & l_e & 6 & -l_e \\ -6 & -l_e & 6 & l_e \end{bmatrix} \frac{1}{12} \tag{29}$$

and

$$\mathbf{K_{24}^{te}} = -\mathbf{K_{34}^{te}} = rk_t \frac{h_b}{2} \begin{bmatrix} -6 & l_e & 6 & -l_e \\ -6 & -l_e & 6 & l_e \end{bmatrix} \frac{1}{12} \tag{30}$$

arise from the coupling between the axial and lateral coordinates. In addition, the contact stiffness matrix is also composed of the elemental matrices

$$\frac{1}{2}\mathbf{K_{44}^{ve}} = \mathbf{K_{55}^{ve}} = \mathbf{K_{66}^{ve}} = -\mathbf{K_{45}^{ve}} = -\mathbf{K_{46}^{ve}} = rk_v \begin{bmatrix} 156 & 22l_e & 54 & -13l_e \\ 22l_e & 4l_e^2 & 13l_e & -3l_e^2 \\ 54 & 13l_e & 156 & -22l_e \\ -13l_e & -3l_e^2 & -22l_e & 4l_e^2 \end{bmatrix} \frac{l_e}{420} \tag{31}$$

which result from the vertical contact stiffness. The elemental electromechanical coupling for the axial coordinates and for the lateral coordinates, respectively,

$$\mathbf{\Theta_2^e} = -\mathbf{\Theta_3^e} = r\frac{d_p E_p w_p}{C_p} \begin{bmatrix} 1 \\ -1 \end{bmatrix} \tag{32}$$

$$\mathbf{\Theta_5^e} = \mathbf{\Theta_6^e} = r\frac{h_{pd} d_p E_p w_p}{C_p} \begin{bmatrix} 0 \\ -1 \\ 0 \\ 1 \end{bmatrix} \tag{33}$$

illustrate the coupling between the mechanical and electrical domains of the piezoelectric elements, and the elemental force

$$\boldsymbol{F_4^e} = -\begin{bmatrix} 6 \\ l_e \\ 6 \\ -l_e \end{bmatrix} \frac{\rho_b A_b l_e}{12} \ddot{v}_0 \tag{34}$$

results from the motion at the beam's base.

2.3 Piezoelectric Vibration Control. To dissipate energy, piezoelectric elements are connected to the resonant shunt shown in Fig. 4. The piezoelectric elements are modeled electrically as the charge generator $q_p = C_p \mathbf{\Theta}^T \eta$ in parallel with capacitance C_p. In the open circuit condition, the system's dynamic response is governed by Eq. (17). When the piezoelectric elements are connected to a shunt with resistance R and inductance L, the mechanical system and the electrical system couple as

$$\begin{bmatrix} \mathbf{M} & \mathbf{0} \\ \mathbf{0}^T & L \end{bmatrix} \begin{bmatrix} \ddot{\eta} \\ \ddot{q}_a \end{bmatrix} + \begin{bmatrix} \mathbf{0} & \mathbf{0} \\ \mathbf{0}^T & R \end{bmatrix} \begin{bmatrix} \dot{\eta} \\ \dot{q}_a \end{bmatrix} + \begin{bmatrix} \mathbf{K^{oc}} & -\mathbf{\Theta} \\ -\mathbf{\Theta}^T & \frac{1}{C_p} \end{bmatrix} \begin{bmatrix} \eta \\ q_a \end{bmatrix} = \begin{bmatrix} \mathbf{F} \\ 0 \end{bmatrix} \tag{35}$$

where $\mathbf{K^{oc}} = \mathbf{K^s} + \mathbf{K^{tv}} + C_p \mathbf{\Theta}\mathbf{\Theta}^T$ is the open-circuit stiffness matrix. In short, Eq. (17) yields the system response with no control, and Eq. (35) yields the response under resonant shunt control. In each case, proportional damping of the form $2\zeta_i \omega_i$ is assumed for

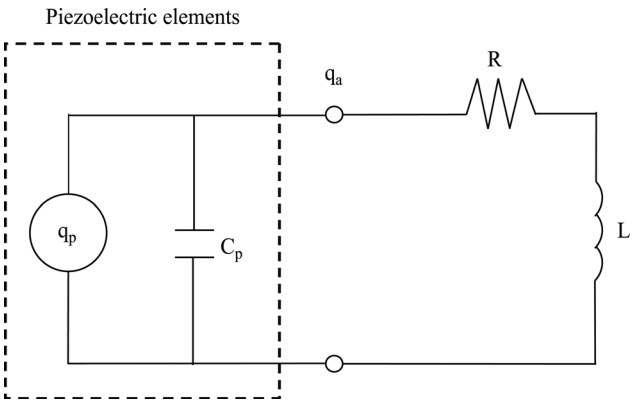

Fig. 4 Schematic of the piezoelectric elements that are connected to a resonant shunt

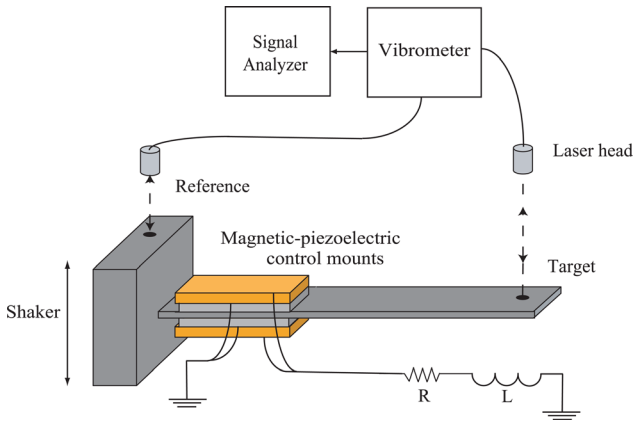

Fig. 5 Illustration of experimental setup of cantilever beam with magnetically mounted piezoelectric elements

the coupled beam and control mounts system (η coordinates), where ζ_i and ω_i are the modal damping ratio and natural frequency of the i^{th} mode.

3 Control Mount Design

Figures 5 and 6 show a 25.4 × 1.27 × 0.32 cm steel cantilever beam (with a free length of 20.3 cm) that was mounted through its support to an electromagnetic shaker (MB Dynamics). A Michelson-style interferometer (Polytec OFV-502 and OFV-3000) measured the velocity of the beam's tip relative to the base; fiber optic leads set paths for the reference and target laser beams. The velocity signal was sent to a dynamic signal analyzer (Hewlett Packard) that generated the frequency response functions. Two magnetic-piezoelectric control mounts were attached to the beam near its base. The piezoelectric elements were connected to an active inductor, which was designed using two op-amps [14,37].

Each control mount was made of a 6.35 × 1.27 × 0.24 cm ceramic piezoelectric element (American Piezo, APC 850 (Navy Type II)) attached with epoxy to one of three different magnetic configurations, which were designed with grade N42 neodymium magnets (K&J Magnetics, Inc.). Figure 7(*a*) illustrates a control mount that used a single 6.35 × 1.27 × 0.16 cm magnetic block, and Figs. 7(*b*)–7(*c*) show control mounts with arrays of alternating magnetic dipoles, which increased the attraction force without increasing the magnet thickness [38]. The rectangular magnet

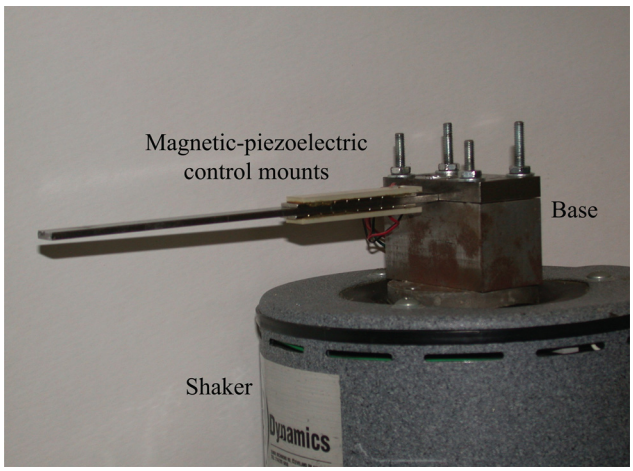

Fig. 6 Experimental setup of cantilever beam with magnetically mounted piezoelectric elements

configuration (Fig. 7(*b*)) was comprised of twenty 0.63 × 0.63 × 0.16 cm block magnets, and the square magnet configuration (Fig. 7(*c*)) of thirty-eight 0.16 × 1.27 × 0.16 cm block magnets. The single and rectangular control mounts each had a mass of 0.025 kg, and the square control mounts had a mass of 0.024 kg.

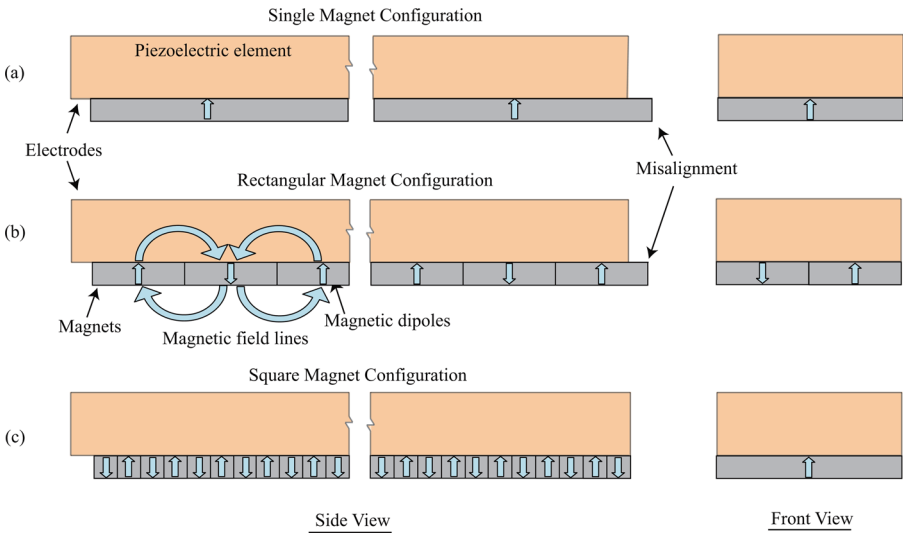

Fig. 7 Illustration of the the different magnetic arrays: (*a*) single magnet configuration, and the alternating dipole configurations of the magnets with (*b*) rectangular and (*c*) square cross sections

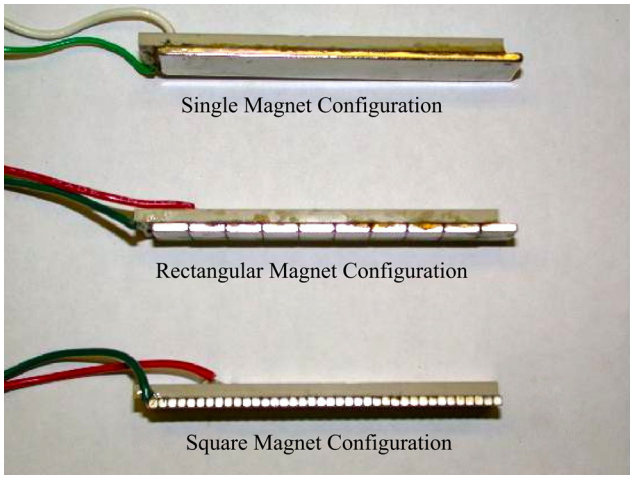

Fig. 8 The control mounts used in experimentation, illustrating the different magnetic array configurations

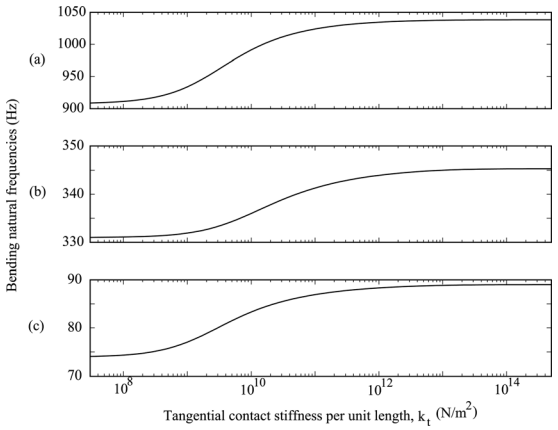

Fig. 9 Illustration of the asymptotic behavior of the (*a*) third, (*b*) second, and (*c*) first bending natural frequencies for different tangential contact stiffnesses per unit length ($k_v = 1\times10^{14}$ N/m^2)

To build the control mounts, the bottom surface of the magnets were first attached to the top surface of a steel block in the desired configuration using their magnetic attraction. Next, the top surfaces of the magnets and the bottom surface of the piezoelectric element were bonded together using epoxy. Once the piezoelectric element was placed on the magnet, weights were placed upon the top surface of the element for 24 h to ensure a strong epoxy bond. In order to ground the bottom electrode, the patches were aligned such that the magnets did not cover the entire electrode surface, as illustrated in Figs. 7 and 8. The magnets and piezoelectric patches were standard ready-made sizes and had fixed lengths, which caused slight misalignment on both ends of the single and rectangular magnet configurations, but only on one end of the square magnet configuration. For example, the single magnet and piezoelectric element were both 6.35 cm long and in order to ground the bottom electrode, a portion of the magnet extended past the length of the element, as illustrated in Fig. 7.

4 Control Mount Influence on Natural Frequencies

The numerical model described in the previous sections was applied to simulate the behavior of the beam with magnetically mounted piezoelectric elements. The electrodes were set to an open circuit condition. With each control mount having approximately the same mass, the natural frequencies of the system were largely influenced by the vertical and tangential contact stiffnesses between the control mounts and the beam. Figure 9 illustrates the manner in which the first three natural frequencies varied for $k_v = 1 \times 10^{14}$ N/m^2 and for various values of tangential contact stiffness, with the control mounts placed at location $l_1 = 0.32$ cm. The torsional stiffness in the model was adjusted such that the simulated natural frequencies of the beam only (no mounts), which were 59 Hz (-1.6%), 362 Hz (1.1%), and 1017 Hz (0.1%), approximated the measured values with the percent error shown. For low contact stiffness ($k_t \leq 10^8$N/m^2), the mounts had minimal influence on the bending natural frequencies, but as the stiffness was increased, the frequencies asymptotically approached those of a beam with perfectly bonded control mounts.

This phenomenon is illustrated further in Fig. 10 which shows the first three bending natural frequencies for different control mount locations on the beam and for various contact stiffnesses in the range 10^7 N/m$^2 \leq (k_t = k_v) \leq 10^{15}$ N/m^2. The system's bending modes closely resembled those of a cantilever beam, as shown in Fig. 10(*a*), and when the control mounts were placed over regions of large modal curvature, they contributed more to the bending energy of the beam for increasing normal and tangential contact stiffnesses. Thus, there was a more pronounced effect on the natural frequencies at those locations. The simulated model accounted for the slight misalignment on both ends of the single and rectangular magnet configurations, and Fig. 10 shows that the measured natural frequencies followed the trends of the simulated model.

The contact stiffnesses k_t and k_v used in the model were approximated by minimizing the root-mean-square percent error

$$e = \text{rms}\left(\sum_{i=1}^{3}\sum_{j=1}^{12}\frac{\omega_i^m(l_{1j}) - \omega_i^s(l_{1j})}{\omega_i^m(l_{1j})} \times 100\right) \tag{36}$$

where ω^m and ω^s are the measured and simulated bending natural frequencies, respectively, and l_{1j} is the location of the control mount. Thus, the error is summed over the first three modes with the control mounts at twelve different locations. A contour plot of

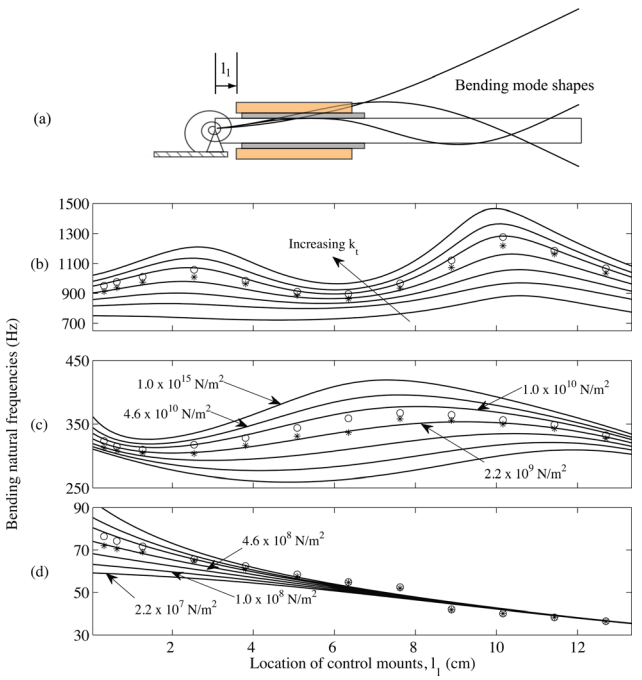

Fig. 10 (*a*) Illustration of the bending mode shapes, and the (*b*) third, (*c*) second, and (*d*) first bending natural frequencies for different control mount positions along the beam and increasing contact stiffness ($k_t = k_v$): simulated (sold lines), single magnet (*), and rectangular (o) configurations

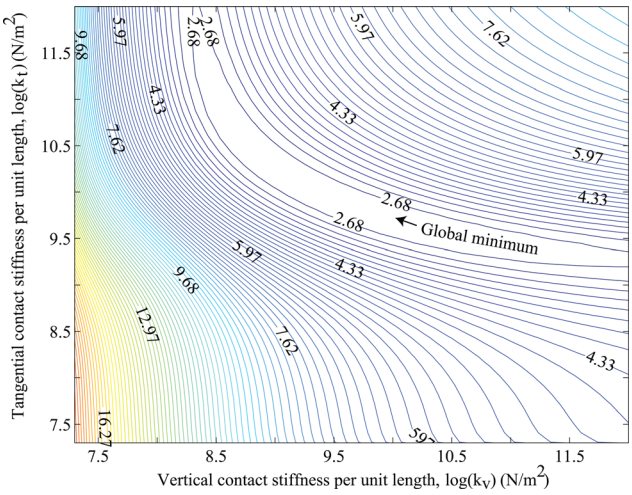

Fig. 11 Contour plot of the simulated natural frequency percent error for the square magnet configuration

Table 2 The contact stiffnesses and resonant shunt parameters used in the simulation

	Control mount configuration		
	Single	Rectangular	Square
Contact stiffnesses			
Tangential, k_t (GN/m^2)	4.45	7.59	5.26
Vertical, k_v (GN/m^2)	1.37	5.93	8.36
Frequency error, e (%)	2.69	2.55	2.47
Contact stiffnesses (adjusted)			
Tangential, k_t (GN/m^2)	2.00	7.59	3.00
Vertical, k_v (GN/m^2)	2.00	5.93	8.00
Frequency error, e (%)	3.09	2.55	2.84
Damping ratio, ζ_1 (%)	2.7	2.5	2.5
Inductance, L (H)	375	346	350
Resistance, R $(k\Omega)$	50	30	30
Capacitance, C_p (nF)	11.0	11.8	11.9
Tip velocity reduction (dB)			
Measured	1.4	3.0	3.0
Simulated	1.4	2.5	2.7
Simulated (adjusted)	1.9	2.5	3.1

the percent error is shown in Fig. 11 for the square magnet control mounts over a range of tangential and vertical contact stiffnesses, with the global minimum ($e = 2.47\%$) shown to illustrate the stiffness values that were chosen. Table 2 shows the stiffness values used in the model, as well as the percent error in the natural frequencies. The simulated natural frequencies were within 2.7% of the measured values for all the control mounts, especially those associated with the square magnet control mounts, as illustrated in Fig. 12. A stronger magnetic bond existed between the rectangular and square magnet control mounts and the beam, compared to that of the single magnet control mount, as illustrated by the increase in contact stiffnesses.

5 Vibration Control Performance

5.1 Experimental Results Comparison. The magnetic-piezoelectric control mounts attenuated vibration even without perfect bonding. The measured and simulated tip velocity responses for the three different control mounts with no control and with resonant shunt control are shown in Fig. 13 for two different sets of stiffness values. Figures 13(*a*)–13(*c*) show the

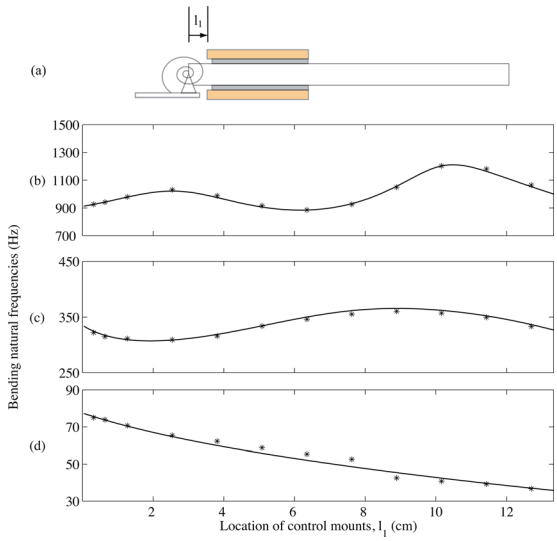

Fig. 12 (*a*) Illustration of the beam with the square magnet control mount design, and the (*b*) third, (*c*) second, and (*d*) first bending natural frequencies: simulated (solid lines) and measured (*)

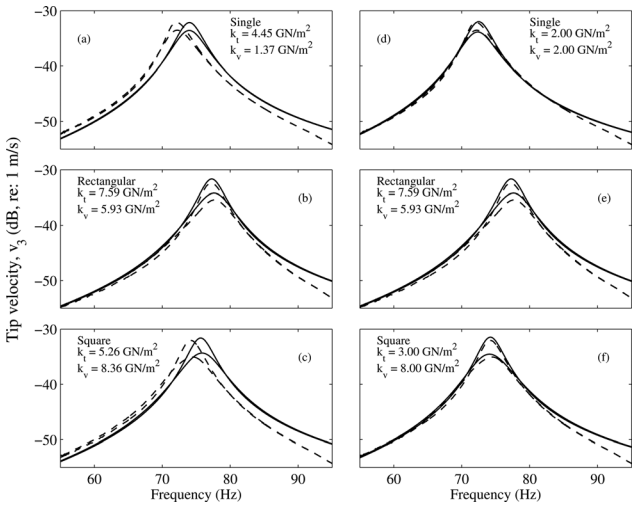

Fig. 13 The simulated (solid) and measured (dashed) tip velocity of the system with and without resonant shunt control for the three different control mounts

results for the contact stiffnesses developed Sec. 4. The system was excited with sinusoidal base excitation with peak amplitude $\ddot{v}_0 = 0.30\ \mathrm{m/s^2}$, the piezoelectric elements were attached at location $l_1 = 0.32$ cm, and the electrodes were set to an open circuit condition. The electrical and stiffness parameters used in the simulation and experiments are shown in Table 2, as well as a summary of the vibration control results. The damping ratio of the each configuration's cantilever mode was measured using the half-power point method. The optimum inductance and resistance were computed [6], but were adjusted to the values in Table 2 to compensate for the large inherent resistance of the active inductor. The measured tip velocity under resonant shunt control was reduced by 1.4 dB using the control mounts with the single magnet configuration, and by 3.0 dB with the rectangular and square magnet configurations. In simulation, reductions of over 1.4 dB, 2.5 dB, and 3.0 dB were seen using the single, rectangular, and square magnet configurations, respectively.

The vibration reduction of the resonant shunt technique is dependent upon the tuning of the electrical circuit's resonance to the

beam's resonant frequency. As Figs. 13(*a*) and 13(*c*) illustrate, the simulated resonances were slightly higher than measured for the single and square control mount configurations, which has a negative effect on the amount of attenuation provided by the resonant shunt as a result of this mistuning. Thus, the simulations were conducted with an adjusted set of contact stiffnesses which were tuned to match the simulated resonances with those measured, as shown in Figs. 13(*d*) and 13(*f*). The results show that tip velocity reduction was increased from 1.4 dB to 1.9 dB for the single magnet configuration, and from 2.7 dB to 3.1 dB for the square magnet configuration. Figures 13(*b*) and 13(*e*) are the exact same result, since the stiffness values determined in Sec. 4 for the rectangular control mounts already provided good correlation. It should be noted that there was a rocking mode of the beam-shaker system that occurred above 95 Hz, which accounts for the off resonance measured response diverging from simulation above approximately 85 Hz.

The difference in the amount of vibration reduction for each of the control mounts is likely from several sources. Uneven contact at the beam-magnet interface could have diminished performance for the large magnet configuration. That is to say, the smaller magnets in the rectangular and square magnet configurations might conform to the beam's imperfect surface better than the single magnet. This characteristic, along with the single magnet configuration's lower magnetic attraction force, may have resulted in slip occurring between the beam and control mounts over a portion of the beam's vibration cycle, which would have diminished the performance. This will be discussed in more detail in the Sec. 5.2. The measured reductions (3.0 dB) also did not increase for the square magnet configurations compared with the rectangular configurations, which was expected based on the simulated results. Measurement noise, which made it difficult to distinguish the 7% model difference between the two configurations, could have caused this discrepancy.

The control mount's performance was also highly affected by the large inherent damping in the system without any control mounts attached (beam only), which was measured to be approximately 2.5% using the half-power point method. For example, consider that for large contact stiffnesses ($k_t = k_v \geq 10^{15}\text{N/m}^2$) that approximated a perfect bond, the resonant shunt technique still only provided about 3.6 dB attenuation in simulation. In practice, piezoelectric vibration control typically provides reductions of 15–25 dB for lightly damped systems [6,14]. For such a system, it is expected that the control mounts would dissipate more energy from the system, which will be discussed more in Sec. 5.3.

Nonetheless, in both experiment and simulation, the magnetic-piezoelectric control mounts reduced the beam's tip velocity by 3.0 dB without a permanent bond to the beam. Furthermore, the results illustrate that while using the same piezoelectric elements, the control mounts with the larger interfacial contact stiffnesses attenuated more vibration.

5.2 Sticking Interface Assumption. The magnetic-piezoelectric control mount's ability to attenuate vibration is dependent upon the strength of the magnetic bond between the beam and the control mounts. This is also an important parameter in determining whether the contact interface is sticking or slipping. A pulley assembly was designed to directly measure the slip force f_{sl} between the different control mounts and the beam. Compared to the single magnetic block, slip occurred for the rectangular and square magnet configurations for slip forces 8 and 12.5 times larger, respectively, as shown in Table 3.

The normal force between the beam and magnets were also determined using ANSYS, and the results are shown in Table 3. In the ANSYS model, the magnets and beam were modeled with 8-noded elements (SOLID96) with the magnetic properties and dimensions given in Table 1. The piezoelectric elements were not included in the model since they are nonmagnetic and were assumed to not affect the distribution of the magnetic flux lines.

Table 3 Comparison of the control mount's simulated normal force and measured slip force

	ANSYS simulation		Measured	
Control mount configuration	Normal force (N)	Ratio	Slip force, f_{sl} (N)	Ratio
Single	33.4	1.0	8.9	1.0
Rectangular	244.8	7.3	71.2	8.0
Square	382.7	11.5	111.3	12.5

The rectangular and square magnet configurations had normal forces that were 7.3 and 11.5 times larger, respectively, than the single magnetic block of the same size. Assuming that the coefficient of friction between the beam and magnets is the same for each configuration, the ratio of the normal forces and slip forces should be equal. The discrepancies between the simulated and measured force ratios may be attributed to the differences in how each control mount conforms to the beam's surface.

The distinction between sticking and slipping at the interface of the control mounts and the beam is dependent upon the tangential relative displacement vector

$$\mathbf{r_t} = \boldsymbol{\eta_2} - \boldsymbol{\eta_1} + \mathbf{R}\left(\frac{h_b}{2}\boldsymbol{\eta_4} + h_n\mathbf{n_5}\right) \tag{37}$$

where the matrix

$$\mathbf{R} = \begin{bmatrix} 0 & 0 & 0 & 0 & 0 \\ 0 & 1 & 0 & 0 & 0 \\ 0 & 0 & 0 & 0 & 0 \\ 0 & 0 & 0 & 1 & 0 \\ 0 & 0 & 0 & 0 & \ddots \end{bmatrix} \tag{38}$$

is used to extract the nodal rotations. The model specifies that the interface only experiences sticking, and as a result, the condition $(\mathbf{r_t})_\mathbf{i} \leq S_o$ must be satisfied at each node, where the parameter $S_o = f_{sl}/(k_t l_m)$ denotes the relative displacement at which slip commences [28,30]. Figure 14 shows the maximum relative displacement variation for different tangential contact stiffnesses for each of the three different control mounts. The system was excited with base excitation $\ddot{v}_0 = 0.30\ \text{m/s}^2$, the piezoelectric elements were attached at location $l_1 = 0.32$ cm, and frequency responses were calculated over 40 – 140 Hz using the vertical contact stiffnesses determined in Sec. 4. The slip parameter variation is also

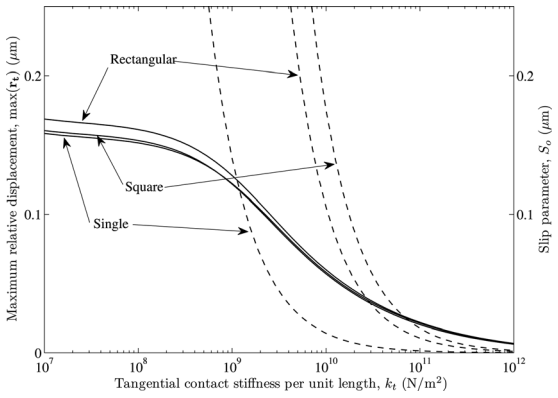

Fig. 14 Comparison of the simulated maximum relative displacements (solid) to the measured slip parameter (dashed) for the three control mounts: single, rectangular, and square

shown in Fig. 14 using the measured slip forces for each control mount.

The results show that the tangential forces between each rectangular and square control mounts and the beam were within the sticking regime ($k_t \approx 3.0 - 8.0 \times 10^9$ N/m^2). However, the relative displacement between the beam and single magnet control mounts exceeded the slip parameter. Thus, the interface experienced a combination of sticking and slipping forces over the beam's vibration cycle. It is interesting to note that even with this small nonlinearity in the system, the linear model still predicted the natural frequencies of the square magnet configuration to within 3% of the measured values. However, the model overpredicted the amount of tip velocity reduction with the resonant shunt. The excitation amplitude is also an important parameter in determining the amount of slipping that occurs at the beam-magnet interface. It is expected that for lower excitation amplitudes, the large magnet control mounts would not experience any slipping and the model would provide a better prediction of the measured reductions. To the contrary, as the excitation amplitude increases beyond what was tested, the displacements and curvature of the beam will also increase and at some point, the contact interface between the rectangular and square control mounts and the beam will begin to slip. Overall, for the excitation amplitudes tested, the results show that the model accurately captured the dynamic behavior at the contact interface for the rectangular and square magnet control mounts.

5.3 Design Tradeoffs. A tradeoff exists between the vibration reduction performance of the control mounts and the ability to easily remove and replace them. This is illustrated in Fig. 15, which demonstrates the tip velocity reduction variation for different contact stiffnesses ($k_t = k_v$) and damping ratios. The shunt resistance was set to the experimental value ($R = 30$ kΩ) and the inductance was varied such that the electrical resonance was tuned to the system's fundamental mode. For low values of vertical contact stiffness ($k_v \leq 10^7$ N/m^2), the control mounts had poor coupling with the beam and, as a result, there was no vibration reduction exhibited with the control mounts. As the contact stiffness increased, the control mounts conformed more with the beam thus producing more strain in the piezoelectric elements and a larger reduction in the beam's tip velocity. For the rectangular and square control mounts ($k_v \approx 5.0 - 8.0 \times 10^9$ N/m^2), the reductions (2.5–3.1 dB) were comparable to the reduction (3.6 dB) exhibited for perfectly attached control mounts ($k_t = k_v = 10^{15}$ N/m^2). Figure 15 also demonstrates that for a lightly damped system ($\zeta = 0.5\%$), these vibration control mounts would have provided an approximate 10 dB reduction in the beam's tip velocity.

A degradation in performance is also introduced by inserting a stiff and thick magnet layer in between the piezoelectric element

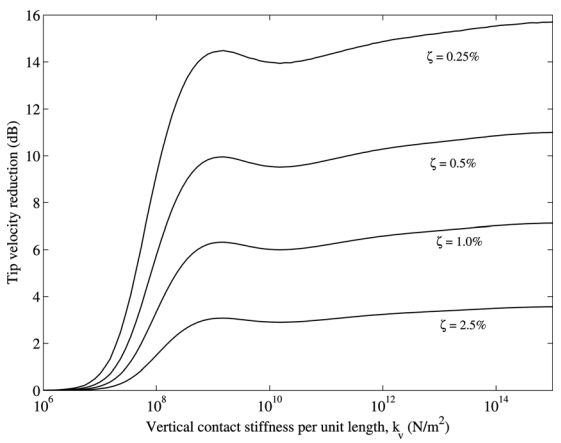

Fig. 15 Tip velocity reduction using resonant shunt control for various contact stiffnesses and damping ratios

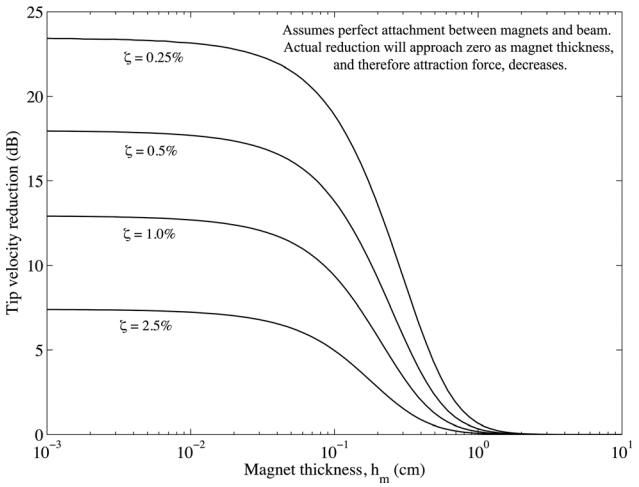

Fig. 16 Tip velocity reduction using resonant shunt control for various magnet thicknesses and damping ratios, assuming perfect attachment between magnets and beam. Actual reduction approach zero as magnet thickness, and therefore attraction force, decreases.

and the beam. Figure 16 shows the tip velocity reduction for different magnet thicknesses and damping ratios. It was assumed that the control mounts were perfectly attached ($k_t = k_v = 10^{15}$ N/m^2) to the beam. Again, the shunt resistance was set to the experimental value ($R = 30$ kΩ) and the inductance was varied such that the electrical resonance was tuned to the system's fundamental mode. For small magnet thicknesses ($h_m \leq 0.01$ cm), the reductions were approximately equal to those of a piezoelectric element perfectly attached to a beam. As the magnet thickness increased, the bending stiffness of the system increased, thereby decreasing the strain in the piezoelectric elements. As a result, the control mounts provided no reduction in the beam's tip velocity. This phenomenon is also apparent from measurements of the generalized electromechanical coupling coefficient k_{31}^2 which, for the current control mounts, was measured to be between 0.26–0.27% based upon the frequency change between short and open circuit conditions [6]. As a comparison, for piezoelectric elements attached directly to a beam using epoxy, the coupling coefficient has been measured to be between 0.65–2.53% [6,14]. The results of Fig. 16 indicate that the addition of the magnets decreased the reduction from 7.4 dB ($h_m \leq 0.01$ cm, $\zeta = 2.5\%$) to 3.1 dB for the square magnet configuration. For a lightly damped system ($\zeta = 0.5\%$), Figs. 15 and 16 indicate that the reduction would have decreased from 17.9 dB to approximately 10 dB with the addition of the magnets. The results demonstrate that the control mounts still provide comparable attenuation albeit not as much when compared to the traditional epoxy mounted piezoelectric elements.

Future work should investigate methods to increase the vibration reduction performance of the control mounts. As noted in Fig. 16, as the magnet thickness decreases, the attraction force will also decrease resulting in decreased vibration reduction. Going forward, research should focus on decreasing the thickness of the magnet layer while still providing adequate attraction force between the beam and magnet. The magnetic attraction force can be increased by using a Halbach array, illustrated in Fig. 17(*a*), which rotates the magnets in a clockwise fashion along the length of the mount [38,39]. The array provides a 40% increase in attachment force over the square magnet configuration. The Halbach design was attempted in this work, but the natural tendency of the magnets to become misplaced, as illustrated in Fig. 17(*b*), caused the ceramic piezoelectric elements to crack and break. In addition, it should be noted that the magnets do not necessarily need to cover the entire piezoelectric element, as Fig. 18 illustrates [25].

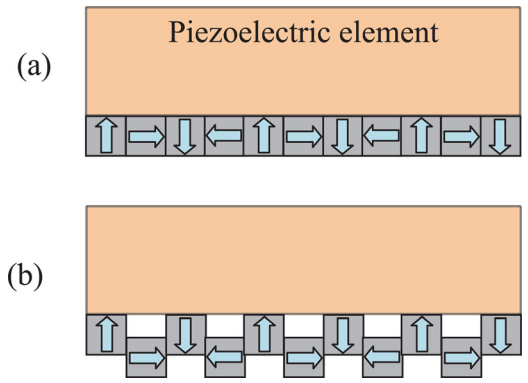

Fig. 17 Illustration of the (*a*) magnetic dipole configuration of a Halbach array, and (*b*) natural orientation of magnets

Fig. 18 Example of a control mount with magnets placed at the ends of the piezoelectric element

This would reduce the bending stiffness of the system while still providing coupling between the beam and the piezoelectric element. Lastly, by reducing the total magnet volume, the weight of the control mounted could be reduced, which would be beneficial for light weight systems such as spacecraft or aircraft.

6 Conclusion

Piezoelectric elements are typically bonded with epoxy to vibrating structures to provide attenuation. In the event that the elements become damaged or if environmental changes alter structural dynamics, removing and relocating the elements is difficult with such a bond. A viable and adaptable alternative is magnetic-piezoelectric control mounts that attach to the structure through their magnetic attraction. In simulation and laboratory measurements, the mounts provided significant attenuation even with an imperfect bond. Furthermore, their performance was improved by increasing the attraction force, which was accomplished using a magnetic array configuration that alternated the magnetic dipoles along the length of the control mounts, while keeping the magnet thickness constant. In summary, the contributions of this work are:

- A novel method for the attachment of piezoelectric elements to vibrating structures was developed and investigated. The magnetic-piezoelectric control mounts are easier to remove and replace should an element become damaged.
- A finite element model was developed to simulate the vibration of a pinned-free beam with attached magnetic-piezoelectric control mounts. The model incorporated the contact stiffness at the beam-magnet interface to analyze the imperfect connection.
- The vibration control mount's performance was enhanced with magnetic configurations that increased the attraction force for a given magnet thickness.
- The work provides direction for future research in spatially-adaptive vibration controllers, which have the ability to attach and detach themselves in real time.

Acknowledgment

This research was sponsored by the Rickover Fellowship Program.

References

[1] Forward, R. L., 1979, "Electronic Damping of Vibrations in Optical Structures," J. Appl. Opt., **18**(5), pp. 690–697.
[2] Uchino, K., and Ishiii, T., 1988, "Mechanical Damper Using Piezoelectric Ceramics," J. Ceram. Soc. Jpn., **96**(8), pp. 863–867.
[3] Lesieutre, G. A., and Davis, C. L., 1991, "Frequency-Shaped Passive Damping Using Resistively-Shunted Piezoceramics," Proceedings of the Conference on Active Materials and Structures, pp. 355–358.
[4] Hagood, N. W., and Crawley, E. F., 1991, "Experimental Investigation of Passive Enhancement of Damping in Space Structures," J. Guid. Control Dyn., **14**(6), pp. 1100–1109.
[5] Davis, C. L., and Lesieutre, G. A., 2000, "An Actively Tuned Solid-State Vibration Absorber Using Capacitive Shunting of Piezoelectric Stiffness," J. Sound Vib., **232**(3), pp. 601–617.
[6] Hagood, N. W., and von Flotow, A., 1991, "Damping of Structural Vibrations With Piezoelectric Materials and Passive Electrical Networks," J. Sound Vib., **146**(2), pp. 243–268.
[7] Wu, S., 1996, "Piezoelectric Shunts With Parallel RL Circuit for Structural Damping and Vibration Control," Proc. SPIE, **2720**, pp. 259–269.
[8] Wu, S., and Bicos, A. S., 1997, "Structural Vibration Damping Experiments Using Improved Piezoelectric Shunts," Proc. SPIE, **3045**, pp. 40–50.
[9] Caruso, G., 2001, "A Critical Analysis of Electric Shunt Circuits Employed in Piezoelectric Passive Vibration Damping," Smart Mater. Struct., **10**, pp. 1059–1068.
[10] Park, C. H., and Inman, D. J., 2003, "Enhanced Piezoelectric Shunt Design," Shock Vib., **10**(2), pp. 127–133.
[11] Clark, W. W., 2000, "Vibration Control With State-Switched Piezoelectric Materials," J. Intell. Mater. Syst. Struct., **11**(4), pp. 263–271.
[12] Richard, C., Guyomar, D., Audigier, D., and Ching, G., 1999, "Semi-Passive Damping Using Continuous Switching of a Piezoelectric Device," Proc. SPIE, **3672**, pp. 104–111.
[13] Richard, C., Guyomar, D., Audigier, D., and Bassaler, H., 2000, "Enhanced Semi Passive Damping Using Continuous Switching of a Piezoelectric Device," Smart Struct. Mater., **3989**, pp. 288–299.
[14] Corr, L., and Clark, W. W., 2002, "Comparison of Low-Frequency Piezoelectric Switching Shunt Techniques for Structural Damping," Smart Mater. Struct., **11**, pp. 370–376.
[15] Corr, L. R., and Clark, W. W., 2003, "A Novel Semi-Active Multi-Modal Vibration Control Law for a Piezoceramic Actuator," J. Vib. Acoust., **125**, pp. 214–222.
[16] Collinger, J. C., and Wickert, J. A., 2007, "Adaptive Piezoelectric Vibration Control With Synchronized Switching," Proceedings of IMECE 2007: 2007 ASME International Mechanical Engineering Congress and Exposition, Seattle, WA, Nov. 11–15, Paper No. IMECE2007-41427, http://dx.doi.org/10.1115/IMECE2007-41427
[17] Collinger, J. C., Wickert, J. A., and Corr, L. R., 2009, "Adaptive Piezoelectric Vibration Control With Synchronized Switching," ASME J. Dyn. Sys. Meas. and Control, **131**, p. 041006.
[18] Fanson, J. L., and Caughey, T. K., 1990, "Positive Position Feedback Control for Large Space Structures," AIAA J., **28**(4), pp. 717–724.
[19] Alkhatib, R., and Golnaraghi, M. F., 2003, "Active Structural Vibration Control: A Review," Shock Vib. Dig., **35**(5), pp. 367–383.
[20] Yan, Y. J., and Yam, L. H., 2002, "Optimal Design of Number and Locations of Actuators in Active Vibration Control of a Space Truss," Smart Mater. Struct., **11**, pp. 496–503.
[21] Crawley, E. F., and Anderson, E. H., 1990, "Detailed Models of Piezoceramic Actuators of Beams," J. Intell. Mater. Syst. Struct., **1**, pp. 4–25.
[22] Agrawal, B. N., and Treanor, K. E., 1999, "Shape Control of a Beam Using Piezoelectric Actuators," Smart Mater. Struct., **8**, pp. 729–740.
[23] Barboni, R., Mannini, A., Fantini, E., and Gaudenzi, P., 2000, "Optimal Placement of PZT Actuators for the Control of Beam Dynamics," Smart Mater. Struct., **9**, pp. 110–120.
[24] Main, J. A., Garcia, E., and Howard, D., 1994, "Optimal Placement and Sizing of Paired Piezoactuators in Beams and Plates," Smart Mater. Struct., **3**, pp. 373–381.
[25] Collinger, J. C., Messner, W. C., and Wickert, J. A., 2008, "Vibration Control With Magnetically Mounted Piezoelectric Actuators," Proceedings of IMECE 2008: 2008 ASME International Mechanical Engineering Congress and Exposition, Boston, MA, Oct. 31–Nov. 6, Paper No. IMECE2008-67369, http://dx.doi.org/10.1115/IMECE2008-67369
[26] Collinger, J. C., 2008, "Adaptive Vibration Control Using Magnetically Mounted Piezoelectric Elements," Ph.D. thesis, Carnegie Mellon University, Pittsburgh, PA.
[27] Hawwa, M. A., Al-Nassar, Y. N., and Al-Oahtani, H. M., 2011, Piezoelectric Damping Device. Patent Application No. US 2011/0084572 A1.
[28] Tangpong, X. W., Wickert, J. A., and Akay, A., 2008, "Distributed Friction Damping of Traveling Wave Vibration in Rods," Philos. Trans. R. Soc. London, **366**, pp. 811–827.
[29] Menq, C. H., Bielak, J., and Griffin, J. H., 1986, "The Influence of Microslip on Vibratory Response, Part 1: A New Microslip Model," J. Sound Vib., **107**, pp. 279–293.
[30] Tangpong, X. W., Wickert, J. A., and Akay, A., 2008, "Finite Element Model for Hysteretic Friction Damper of Traveling Wave Vibration in Axisymmetric Structures," J. Vib. Acoust., **130**(1), p. 011005.
[31] Girhammer, U. A., and Gopu, V. K. A., 1993, "Composite Beam-Columns With Interlayer Slip—Exact Analysis," J. Struct. Eng., **119**, pp. 1265–1282.

[32] Heuer, R., and Adam, C., 2000, "Piezoelectric Vibrations of Composite Beams With Interlayer Slip," Acta Mech., **140**, pp. 247–263.
[33] Wu, Y., Xu, R., and Chen, W., 2007, "Free Vibrations of the Partial-Interaction Composite Members With Axial Force," J. Sound Vib., **299**, pp. 1074–1093.
[34] Hagood, N. W., Chung, W. H., and von Flotow, A., 1990, "Modelling of Piezoelectric Actuator Dynamics for Active Structural Control," J. Intell. Mater. Syst. Struct., **1**(1), pp. 327–354.
[35] IEEE, 1988, *An American National Standard: IEEE Standard on Piezoelectricity*, The Institute of Electrical and Electronics Engineers, Inc., New York, NY.
[36] Becker, E. B., Carey, G. F., and Oden, J. T., 1981, *Finite Elements: An Introduction*, 1st ed., Vol. 1, Prentice-Hall, Inc., Englewood Cliffs, NJ.
[37] Hollkamp, J. J., and Starchville, T. F., Jr., 1994, "A Self-Tuning Piezoelectric Vibration Absorber," J. Intell. Mater. Syst. Struct., **5**, pp. 559–566.
[38] Trumper, D. L., Williams, M. E., and Nguyen, T. H., 1993, "Magnet Arrays for Synchronous Motors," *Industry Applications Society Annual Meeting, Conference Record of the IEEE*, Vol. 1, pp. 9–18.
[39] Jang, S. M., Lee, S. H., and Jeong, S. S., 2002, "Characteristic Analysis of Eddy-Current Brake System Using the Linear Halbach Array," IEEE Trans. Magn., **38**(5), pp. 2994–2996.